SPATIAL AND TEMPORAL EVOLUTION OF SOFT AND HARD X-RAY EMISSION IN A SOLAR FLARE

MARCOS E. MACHADO

Observatorio de Física Cósmica – CNIE, 1663 San Miguel, Argentina

ANDRÉ DUIJVEMAN

Space Research Laboratory of the Astronomical Institute at Utrecht, The Netherlands

and

BRIAN R. DENNIS

Laboratory for Astronomy and Solar Physics, NASA Goddard Space Flight Center, Greenbelt, Maryland, U.S.A.

(Received 5 July; in revised form 24 November, 1981)

Abstract. We study the spatial and temporal characteristics of the 3.5 to 30.0 keV emission in a solar flare on April 10, 1980. The data were obtained by the Hard X-ray Imaging Spectrometer aboard the Solar Maximum Mission Satellite. It is complemented in our analysis with data from other instruments on the same spacecraft, in particular that of the Hard X-ray Burst Spectrometer.

Key results of our investigation are: (a) Continuous energy release is needed to substain the increase of the emission through the rising phase of the flare, before and after the impulsive phase in hard X-rays. The energy release is characterized by the production of hot ($5 \times 10^7 \lesssim T \lesssim 1.5 \times 10^8$ K) thermal regions within the flare loop structures. (b) The observational parameters characterizing the impulsive burst show that it is most likely associated with non-thermal processes (particle acceleration). (c) The continuous energy release is associated with strong chromospheric evaporation, as evidenced in the spectral line behavior determined from the Bent Crystal Spectrometer data. Both processes seem to stop just before flare maximum, and the subsequent evolution is most likely governed by the radiative cooling of the flare plasma.

1. Introduction

We present in this paper an analysis of the temporal and spatial development of the 3.5 to 30.0 keV X-ray emission in a solar flare which occurred on 1980 April 10, in active region NOAA 2372.

The X-ray images have been obtained by the Hard X-Ray Imaging Spectrometer (HXIS) aboard the Solar Maximum Mission Satellite (SMM). The instrument capabilities and description have been given by van Beek *et al.* (1980). For preliminary results and details on the instrument performance we refer the reader to papers by Simnett *et al.* (1981), van Beek *et al.* (1981), and Hoyng *et al.* (1981a, b).

The April 10 event has been classified as M4 in the X-ray scale and as a 1N flare in Hα. It occurred in the north–western hemisphere at N12 W42. The Hα event was reported starting at 9^h14^m UT reaching its maximum at 9^h23^m UT. It was accompanied by a microwave burst with a maximum flux of 180 sfu at 8.8 GHz at 9^h21^m. Hoyng *et al.* (1981a) have given a preliminary analysis of the HXIS observations and show the spatial distribution of the emission at the time of the impulsive hard X-ray burst.

Solar Physics **79** (1982) 85–106. 0038–0938/82/0791–0085$03.30.

In Section 2 we give a brief description of the instrument capabilities and operational modes, while in Section 3 to 6 we discuss the flare observations and their interpretation. We also refer in our discussion to complementary data sets obtained by other instruments on board of the SMM, in particular to those obtained by the Hard X-Ray Burst Spectrometer (HXRBS, Orwig *et al.*, 1980), the X-Ray Polychromator (XRP, Acton *et al.*, 1980) and the Ultraviolet Spectrometer and Polarimeter (UVSP, Woodgate *et al.*, 1980).

2. Instrument Capabilities

The Hard X-Ray Imaging Spectrometer (van Beek *et al.*, 1980) is capable of imaging solar flare X-rays in the energy range 3.5 to 30.0 keV. Its spatial resolution is 8″ (FWHM) in its fine field of view which covers an area of 2′40″ by 2′40″ on the Sun, and 32″ in its coarse field of view which sees a larger, 6′24″ by 6′24″ area. Hard X-ray emission in the energy range 16.0 to 30.0 keV is also recorded, without spatial resolution, by the HXIS high energy monitor (HEM) within a 10′ by 10′ (FWHM) area. The temporal resolution varies from 1.5 s to 4.5 s according to the observational mode.

Neighboring pixels of both the coarse and fine fields of view spatially overlap. As a result, a point source will in general cause a response in more than one pixel, unless it is located exactly in the middle of the pixel.

The energy range observed by the HXIS is split up into six energy bands, referred to as band 1 to band 6 (B1 to B6) in the following way, B1: 3.5 to 5.5 keV, B2: 5.5 to 8.0 keV, B3: 8.0 to 11.5 keV, B4: 11.5 to 16.0 keV, B5: 16.0 to 22.0 keV and B6: 22.0 to 30.0 keV.

For further details consult van Beek *et al.* (1980).

3. Pre-Flare Observations

The HXIS observations started at 8^h50^m, at the beginning of the satellite day and about 24 min before the start of the X-ray event. Figure 1 (from Hoyng *et al.*, 1981a) shows the time evolution of the X-ray emission as recorded in all six energy bands.

It can be clearly seen in these plots that the emission in the lower energy bands show small amplitude long-lived intensity fluctuations prior to the impulsive burst observed at high energies. The same type of fluctuations were detected by the Bent Crystal Spectrometer (BCS, see reference to XRP) Ca XIX data and in the N V transition zone line recorded by the UVSP. A qualitative inspection (see also Section 5) of count ratios in the low energy bands shows that the observed variations are most likely due to temperature fluctuations in the region. Similar results are obtained from Ca XIX line ratios which are sensitive to temperature changes (Antonucci, private communication). Examination of the flare region within the HXIS fine field of view shows that the bulk of the emission in these pre-flare brightenings comes from a fairly localized area towards the west of what will subsequently be the main flare region, within and around an area bright in N V which also shows up later during the impulsive phase as a footpoint, in the higher energies (cf. Figure 3 and Section 4).

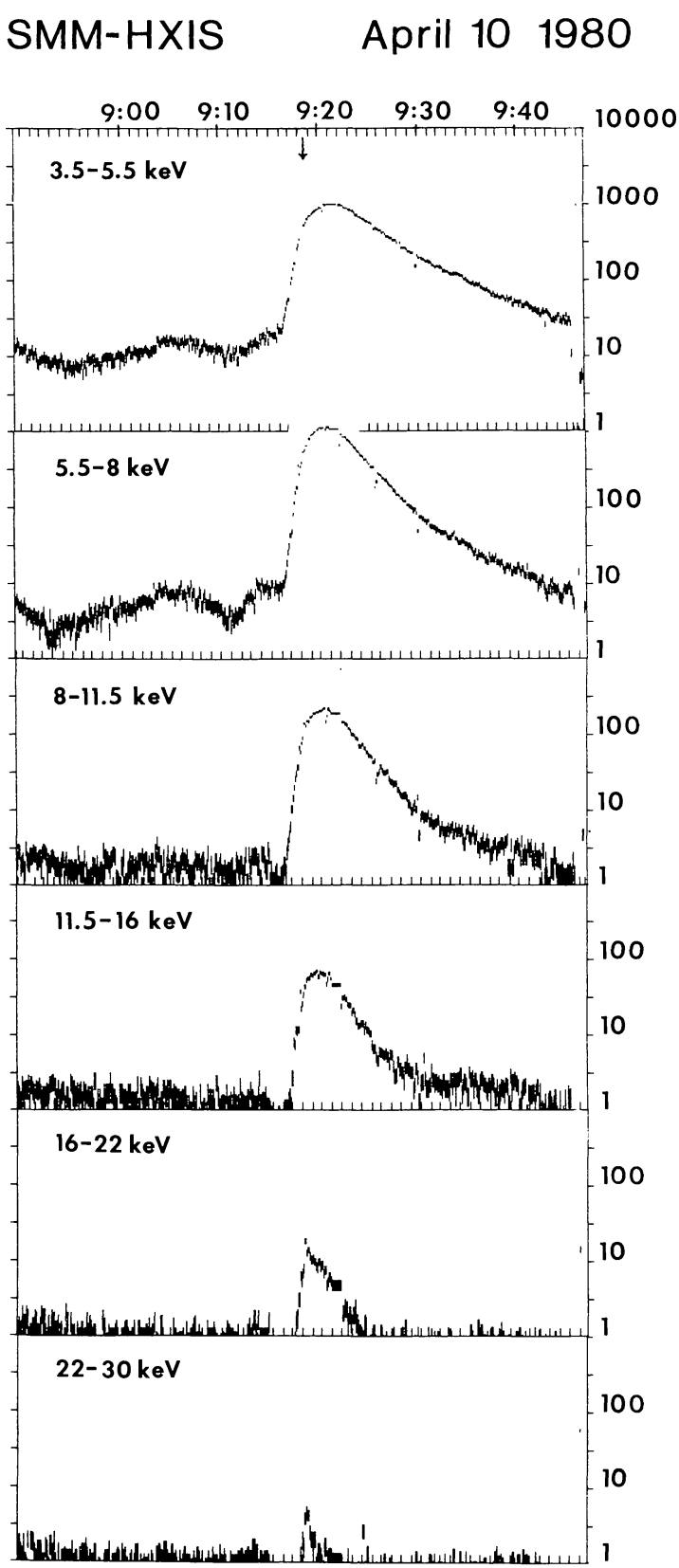

Fig. 1. Intensity-time profiles (in counts per second) of the total flare emission in the HXIS energy bands 1 to 6.

We have found other examples of pre-flare brightenings, and cases in which this type of activity was not immediately followed by stronger flare activity. In all cases the events look like small scale flares and seem to be associated with localized heating within the active region. Their association with EUV brightenings as reported from Skylab (Schmahl *et al.*, 1978; van Hoven *et al.*, 1980) has yet to be confirmed, but considering the association in the April 10 case with N v activity, it is likely that they both represent different manifestations of the same phenomenon.

In the April 10 event the pre-flare brightenings do not seem to be associated with the specific magnetic structure within which the main flare develops. Our results for this flare therefore confirm the existence of a type of pre-flare event discussed by Webb (1980), who found that in 9 out of 17 events pre-flare features did not exactly correspond to the flare site. In a subsequent paper we shall present a detailed study of these type of phenomena and their relation to magnetic structures.

4. Spatial and Temporal Evolution of the X-Ray Emission

In Figure 1 we have shown the temporal evolution of the integrated X-ray emission as recorded by the HXIS. We can now look at the spatial distribution of the intensity as a function of time within the flare region. Figure 2 shows an array of light curves of individual 8″ × 8″ elements in the energy ranges 3.5 to 8.0 keV (Figure 2a) and 16.0 to 30.0 keV (Figure 2b).

To display in better detail the geometry of the region where the flare occurred, we show in Figure 3a a superposition of the HXIS pixels array with a sketch of N v intensities as recorded in a pre-flare raster made by the UVSP. The error in the alignment between both pictures should be less than 5″.

We would now like to single out some characteristics of the X-ray emission shown in Figure 2 and its relationship with transition zone brightenings and magnetic structures (see Figure 3b):

(a) Significant differences appear in the temporal behavior of individual pixels, even in the lower energy bands (Figure 2a). This shows that different magnetic features take part in the flare development.

(b) Impulsive behavior in the high energies is very clear in pixels that overlay N v enhanced regions (i.e., pixels 5, 14, and 17), indicating a preference for stronger impulsive emission at the feet of coronal loops. Weaker emission in the 16 to 30 keV range is however observed during the impulsive burst along pixels connecting these footpoints.

(c) After the impulsive burst, the bulk of the higher energy emission is concentrated along these apparent loop structures.

(d) The post-impulsive burst intensities in the 16 to 30 keV range observed in 'loop pixels' peak during the rise phase of the soft emission and have shorter decay times.

To substantiate these statements we now refer again to Figures 2 and 3. A careful examination of the light curves and the actual images obtained by the HXIS shows that pixels 4, 5, 6 and, in particular, 9 have different behavior than the rest. Pixel 9 shows an earlier flare brightening, a sharper and brighter peak and a faster emission decay.

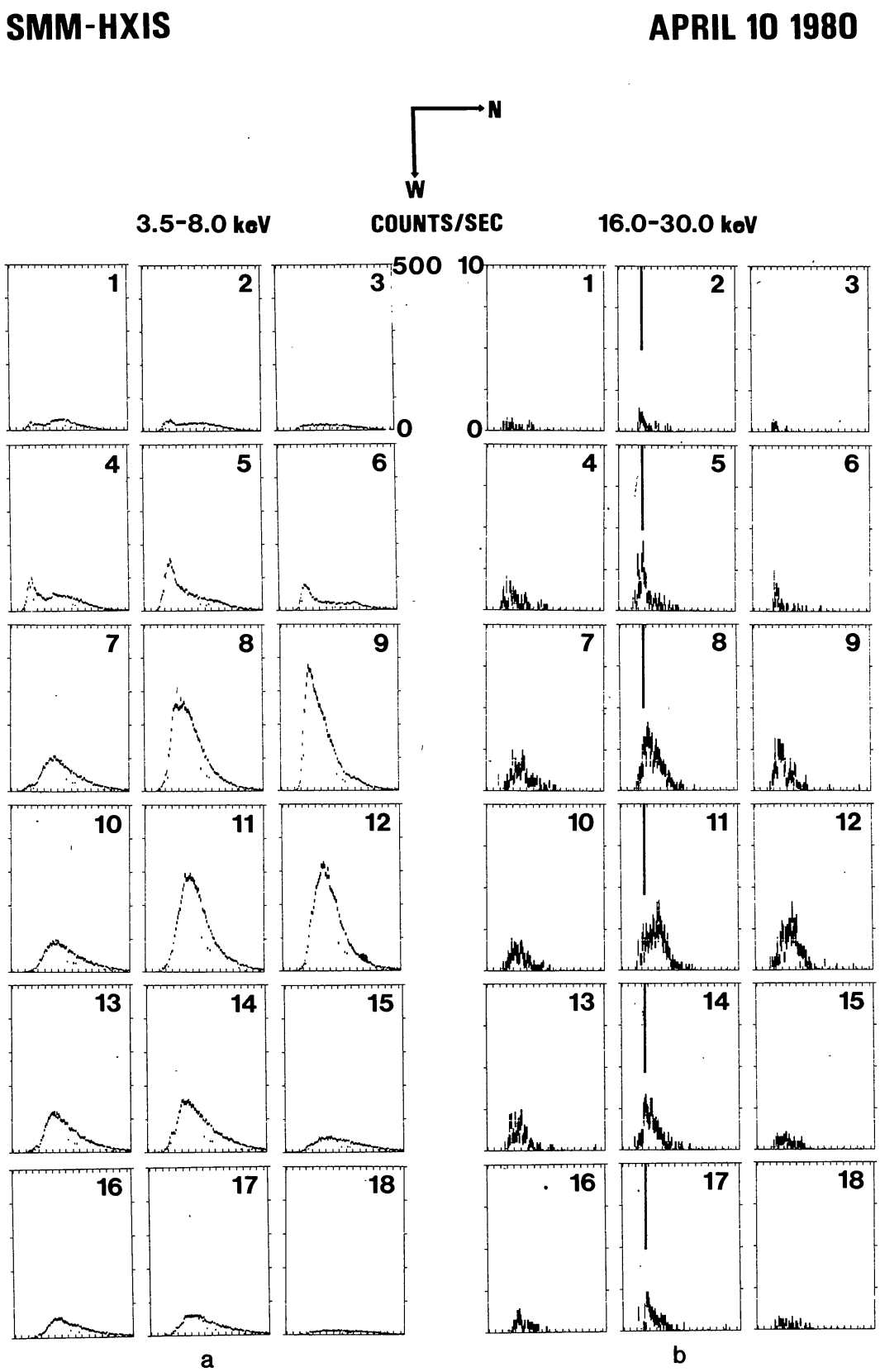

Fig. 2. Array of individual pixels light curves in the HXIS energy bands 1 + 2 (a) and 5 + 6 (b). See text for details. The vertical lines show the time of the hard X-ray peak.

Considering the spatial overlap due to the instrumental response function (cf. Section 2) one can estimate that bright emission is present mainly in pixels 9 and 5, while 4 and 6 intensities are partly due to the overlap. Examination of images and light curves of pixels 9 and 12 shows that no overlap is clearly noticeable, meaning that the region of faster intensity variations is spatially separated from that of pixels showing slower rise-and-fall behavior.

The overlay of HXIS and UVSP images together with a magnetic field map from Marshall Space Flight Center (Figure 3) helps to understand the dissimilar behavior in

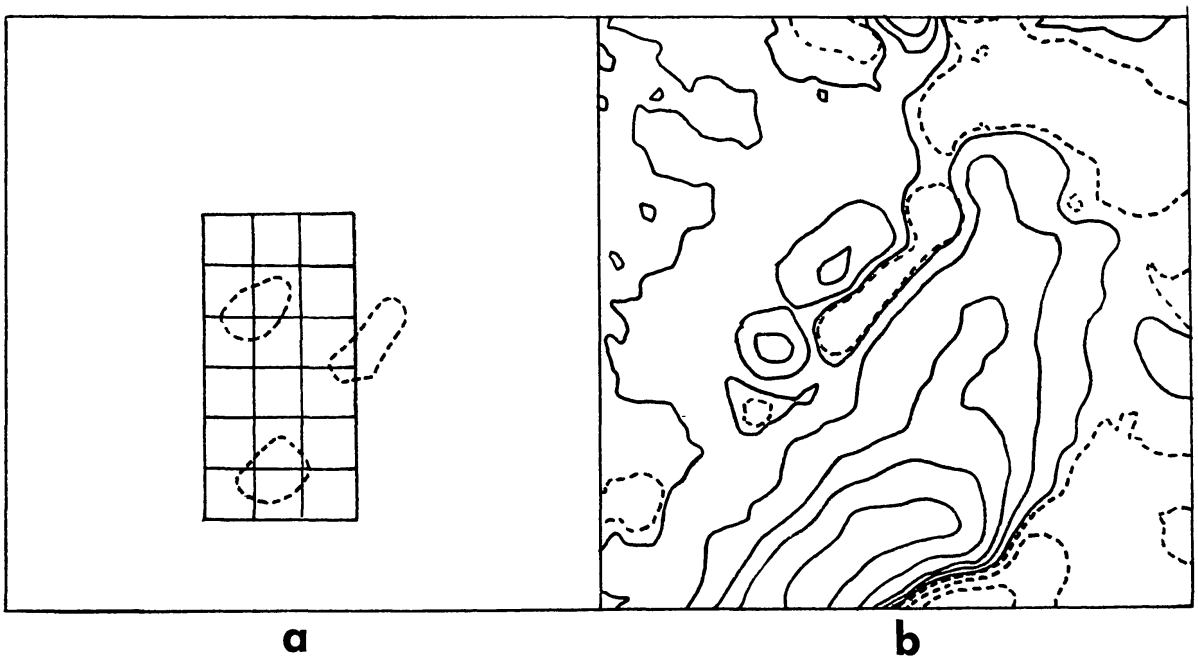

Fig. 3. Overlay of the HXIS pixel array of Figure 2 with a sketch of a pre-flare N v intensity map obtained by the UVSP (a). We show (dashed lines) the regions of maximum intensity in the transition region and (b) the corresponding magnetic field map obtained at the Marshall Space Flight Center. North is to the right and west to the bottom.

different pixels. We see that 5, 14 and, partially, 9 overlay regions of enhanced N v emission which map, as already shown by Skylab, transition zone areas located at the feet of coronal loops. Considering the shape and location of the region in X-rays and N v it seems appropriate to postulate that we observe two loop systems connecting the N v bright areas underneath pixels 5 and 9 in one case and 5 and 14 in the other (note also that projection effects due to the position of the flare on the Sun, W 43, should distort the image somewhat). This physical separation shows that the flare process is not constrained to a single loop geometry, even though the April 10 flare is not an extended long-enduring event associated with a prominence eruption (like others discussed by Švestka, 1976; Pallavicini and Vaiana, 1980; Hoyng *et al.*, 1981b).

The behavior of the integrated flare emission in the 16 to 30 keV range is shown in Figure 4. A sharp maximum (FWHM = 30 s) occurs at $9^h18^m37^s$, preceeded by an increase over a period of about one minute and followed by a weaker tail lasting for several minutes. A similar behavior is seen in the HXRBS data within the energy range

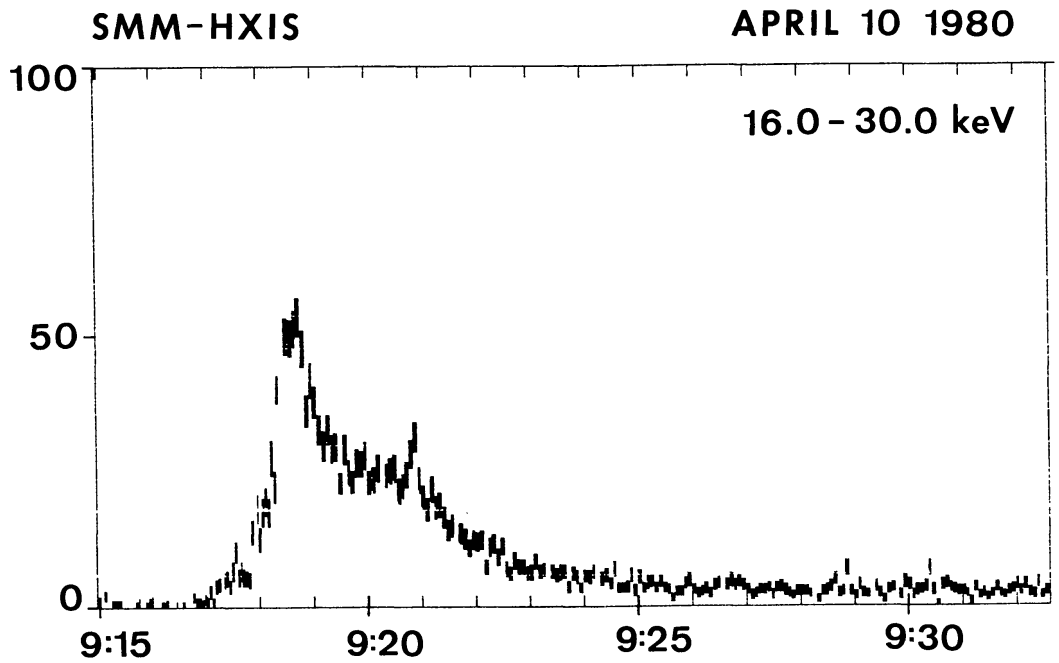

Fig. 4. Intensity-time profile (in counts per second) of the integrated high energy (16 to 30 keV) flare emission as recorded by the HXIS. Note the slow rise in the emission starting already at $\approx 9^h17^m$ and the tail after the impulsive burst. A second, weaker, impulsive feature is superimposed over the tail.

25 to 50 keV, while at higher energies only the impulsive burst is seen. A second, much weaker burst, is observed by the HXRBS at $9^h20^m50^s$ which is also apparent in the HXIS data and corresponds to the peak time in pixel 11 at the higher energies.

At high energies (Figure 2b) we find appreciable count rates in most of the pixels that are also bright in the 3.5 to 8.0 keV range. The emission in pixels *not associated* with N V bright regions (i.e., loop pixels) show a gradual rise and fall behavior in the emission, peaking before the maximum in the soft channels and decaying faster than these. The maximum high energy count rate in these pixels occurs between 30 and 60 s *after* the impulsive burst at $9^h18^m37^s$.

Pixels that *overlay* N V *bright regions* (i.e., footpoint pixels) have a different behavior. They show sharp maxima at the time of the impulsive burst, followed by a steep decay and an emission tail weaker than that of other pixels. At the time of the impulsive burst, the ratio between the count rates of footpoints to loop pixels is $\geq 2:1$ in the 16 to 30 keV range and $\approx 1:1$ in band 4 (11.5 to 16.0 keV). The spatial overlap tends to smooth brightness contrasts and it is enhanced at high energies where the FWHM should be larger than the nominal 8″. Therefore, impulsive brightenings seem to occur preferentially at the feet of coronal loops, confirming the results of Hoyng *et al.* (1981a, b).

The UVSP also recorded high time resolution N V intensity variations within a small (21″ × 21″) raster centered around the western footpoint (i.e., underneath pixels 14 and 17). Its light curve also shows an impulsive brightening co-temporal with that in the hard X-rays, confirming the spatial relationship between chromospheric kernel enhancements and hard X-ray brightenings (see Hoyng *et al.*, 1981b).

It is interesting to note that no clear trace of impulsive burst behavior can be seen in pixel 9 or its neighbors towards the north, although they also overlay a region of enhanced

N v intensity. Following upon our conclusion that the emission in this pixel corresponds to that of a discrete magnetic structure, we conclude that the impulsive burst phenomena seem to be concentrated in a single magnetic structure connecting pixels 5 and 14. On the other hand, considerable high energy emission is seen in pixels 5 and 9 prior to the impulsive burst, significantly above the average level in the other pixels, showing that much of the pre-burst enhancement of Figure 4 originates in this region.

It is also worth noticing that neighboring loop pixels like 8 and 11 show different times of maxima in both the low and high energy bands. While during the impulsive phase their intensities are about equal, pixel 8 peaks in the high energies at $\approx 9^h19^m30^s$ while 11 peaks at $\approx 9^h20^m40^s$. In the low energies the corresponding peak times are $\approx 9^h20^m20^s$ and $9^h21^m40^s$, but they show fairly broad maxima that overlap in time.

5. Physical Parameters

At these early stages of data analysis it is still premature to perform a pixel by pixel spectral analysis of the fine field of view data. Such an exercise should await a detailed study of the instrument transmission characteristics. Therefore in the following analysis we shall confine ourselves to the study of the emission in the coarse field of view elements overlying the main flare region, i.e., integrating over all fine pixels shown in Figure 2 plus 12 more pixels not shown in that figure because of their low emission levels. In doing so we can still work our way back and identify intensity features as corresponding to individual pixels of the fine field of view.

The physical parameters are obtained from the results provided by a computer program referred to as 'the count rate prediction program' (CRPP, see van Beek *et al.*, 1981). The CRPP folds an assumed flare spectrum through HXIS and predicts the count rates in each of the six energy bands. Bot thermal and power-law type of spectra can be handled. The thermal spectrum is computed for a plasma in ionization equilibrium and the predicted count rates reflect the theoretical intensities of bremsstrahlung, resonance and recombination line emission of a plasma at a given temperature, according to the method of Mewe and Gronenschild (1981).

5.1. Temperature and Emission Measure of the Softer X-Ray Plasma

In Figure 5 we show the temperature (T) and emission measure (EM) of the soft X-ray emitting plasma as derived from the intensities of the HXIS low energy bands 1 and 3. We have included a point in the graph which corresponds to a determination from the combination of the observed count rates ratios in bands 1, 2, and 3 from a long integration period (380 s) over the crest of one of the pre-flare brightenings. Although the T and EM values at this time have large statistical uncertainties, the T-values obtained are significantly larger than those derived in typical non-flaring conditions as recorded in other data sets. It therefore shows that the brightenings are due to localized (cf., Section 3) temperature enhancements within the active region.

The temperature and emission measure values of Figure 5 show the classical behavior of soft X-ray plasmas, a temperature peak followed by a maximum in EM and a slow

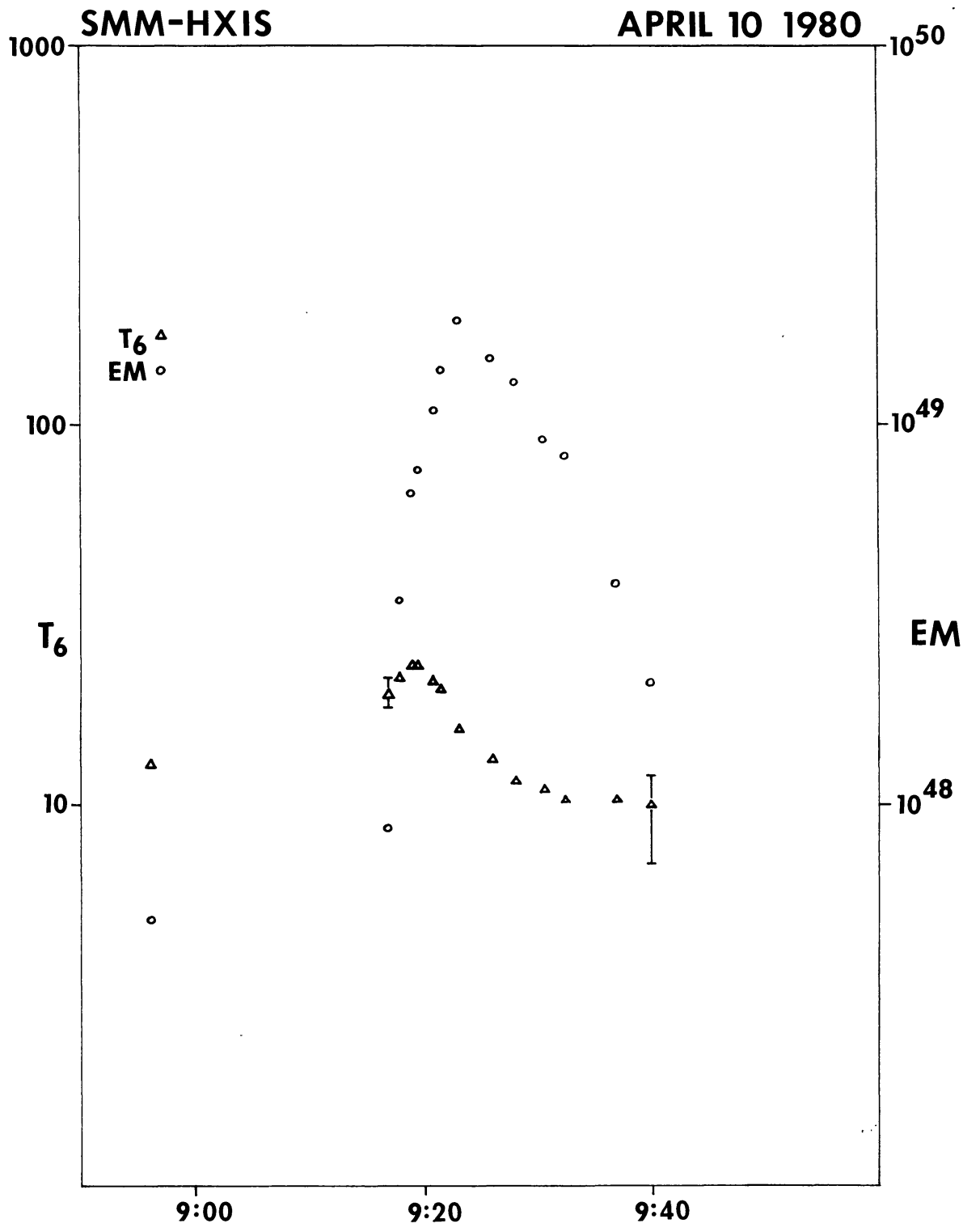

Fig. 5. Variation of temperature (in millions of degrees) and emission measure of the soft plasma as function of time deduced from the HXIS low energy bands.

decay in both during the late phases of the flare. Both T and EM represent spatial averages of the actual physical conditions in the inhomogeneous flare structure and are just appropriate parameters that approximately describe the shape of the observed spectrum. Ca XIX data give lower temperatures and higher emission measures during the

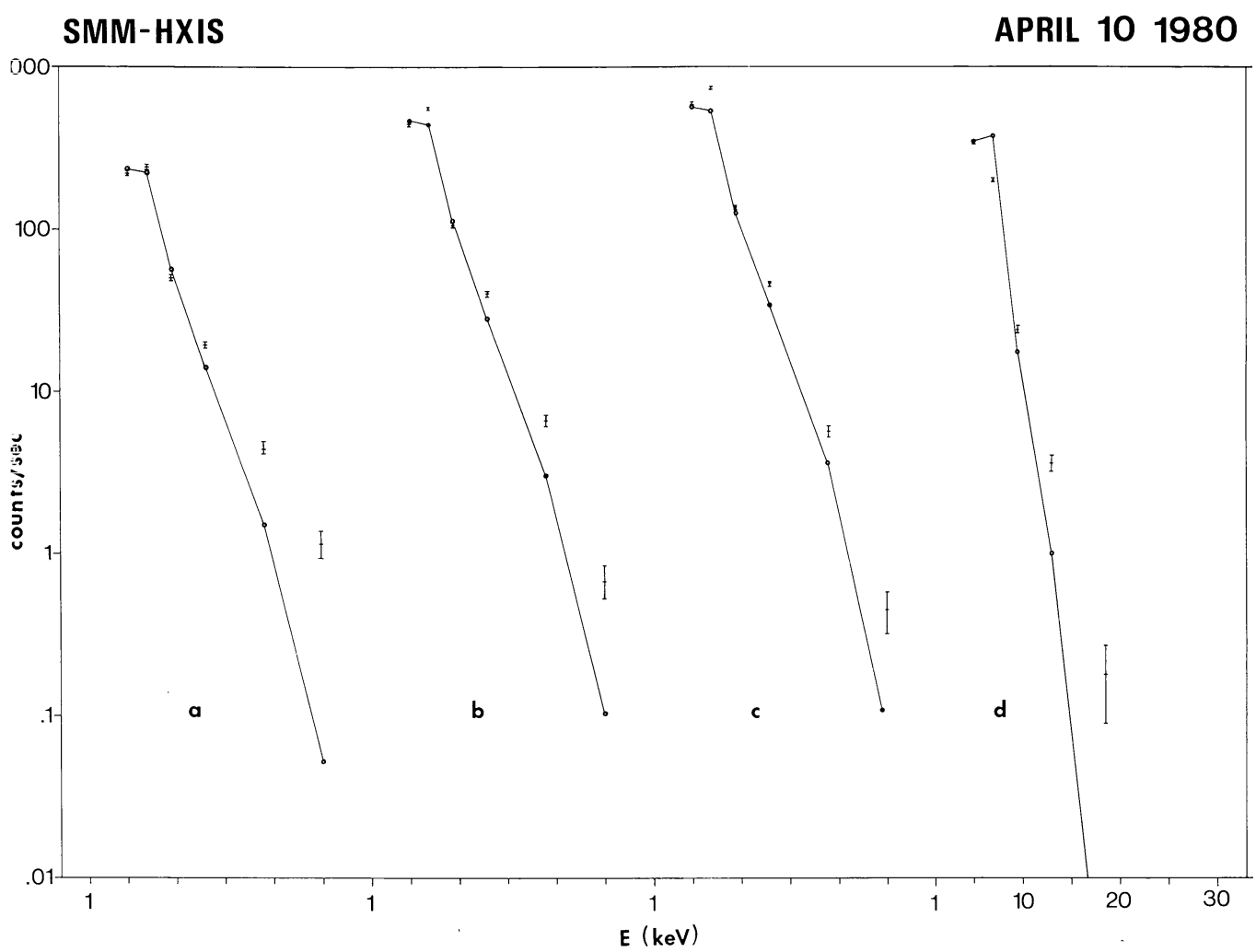

Fig. 6. Observed count rates compared with CRPP predictions for a plasma with soft X-ray parameters as derived from the HXIS low energy bands 1 and 3.
(a) $t = 9^h18^m01^s$; $T = 2.2 \times 10^7$ K, $EM = 2.2 \times 10^{48}$ cm^{-3}.
(b) $t = 9^h18^m37^s$; $T = 2.2 \times 10^7$ K, $EM = 3.7 \times 10^{48}$ cm^{-3}.
(c) $t = 9^h19^m35^s$; $T = 2.2 \times 10^7$ K, $EM = 5.4 \times 10^{48}$ cm^{-3}.
(d) $t = 9^h26^m43^s$; $T = 1.2 \times 10^7$ K, $EM = 1.5 \times 10^{49}$ cm^{-3}.

peak period (9^h19^m to 9^h24^m, Antonucci *et al.*, 1981) integrated over the 6′ by 6′ field of view of the BCS, pointing out the existence of large amounts of plasma at low temperatures.

Figure 6 shows a comparison between observed count rates and CRPP predictions at four relevant times. Considering that some discrepancies in band 2 can be qualitatively understood as due to the influence of emission lines from low-T plasmas, such as seen in BCS Ca XIX data, the agreement between observed and predicted rates is reasonably good in the low energy bands.

Significant discrepancies do however appear in the high energies, where the observed number of counts is much larger than predicted.

The discrepancy in band 2 can be qualitatively understood considering the influence of emission lines from low temperature plasmas as seen by the BCS Ca XIX data. At

temperatures between 1.0×10^7 to 1.6×10^7 K the relative contribution of line emission in B2 is very important compared to that of the continuum, producing a counting rate larger than in B1, as shown in Figure 6d where we have plotted the prediction for a 1.25×10^7 K plasma and where the discrepancy in B2 is now reversed (predicted values larger than observed), probably due, again, to the multithermal character of the region and the presence of even lower temperature plasmas within the field of view (at $T < 10^7$ K B1 counting rates are larger than in B2). A similar effect has been observed in the BCS data, where lower temperatures are generally inferred from Ca XIX than from Fe XXV. The HXIS temperatures are generally in good agreement with those derived from Fe XXV.

The possibility of having lower temperature plasmas within the flare region does not alter the fact that strong discrepancies are found in the predicted and observed count rates at high energies.

5.2. Analysis of the Hard X-Ray Emission

The high counting ratios observed by the HXIS at energies above 11.5 keV, together with those recorded by the HXRBS, can be due to bremsstrahlung emission from thermal plasmas at high temperatures or from a thick target process due to accelerated particles (Peterson and Winkler, 1959; Brown, 1971, 1972; Lin and Hudson, 1976; Crannell *et al.*, 1978; Elcan, 1978). It is generally accepted that the shape of the spectrum does not give unequivocal evidence to distinguish between these two different types of processes (see e.g., Emslie and Brown, 1980, Brown *et al.*, 1980).

Looking now at the HXIS observations, we find that the excess brightness observed above 11.5 keV can be explained, as usual, by thermal contribution from a high-T, low-EM plasma or by postulating a power-law tail extension of the low temperature softer spectrum. In Table I we give the best fit parameters for both the two-temperature and power-law assumptions at various stages through the evolution of the hard X-ray emission. Integrations over ≈ 26 s were made in all cases, to increase the count statistics in the high energy bands. We also show the temperatures derived from similar thermal

TABLE I

Physical parameters and spectral indices derived from the HXIS and HXRBS data

	HXIS					HXRBS		
Time (UT)	Low-T (K)[a]	EM (cm^{-3})[a]	High-T (K)[b,c]	EM (cm^{-3})[b,c]	γ	High-T (K)	EM (cm^{-3})	γ
$9^h17^m40^s$	2.1×10^7	1.5×10^{48}	(2.4×10^8)	(1.2×10^{45})	(≈ 3)	1.0×10^8	6.0×10^{45}	6.3
9 18 01	2.2×10^7	2.2×10^{48}	1.6×10^8	5.0×10^{45}	3.5	1.2×10^8	1.0×10^{46}	6.2
9 18 37	2.4×10^7	3.7×10^{48}	9.0×10^7	1.7×10^{46}	5.0	1.8×10^8	5.8×10^{45}	5.4
9 19 35	2.3×10^7	5.3×10^{48}	5.6×10^7	4.6×10^{46}	>7.0	$(<10^8)$	(6.4×10^{46})	7.2

[a] Best-fit parameters for the low-temperature component.
[b] Best-fit parameters for the high-temperature component.
[c] Numbers between parentheses are uncertain (see text).

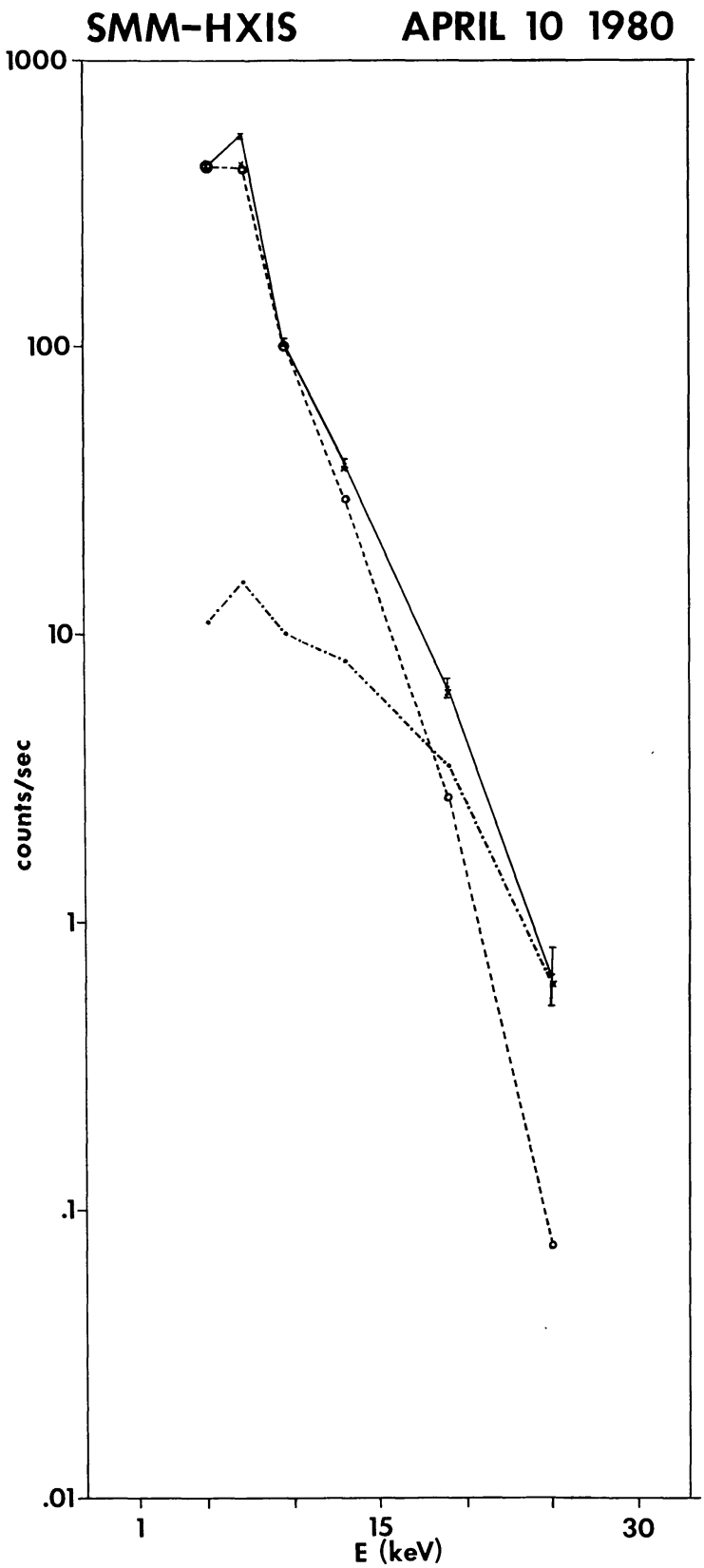

Fig. 7. Two-temperature fit to the HXIS observations at $9^h19^m35^s$. The physical parameters are: low-temperature (dashed line) $T = 2.2 \times 10^7$ K, $EM = 5.3 \times 10^{48}$ cm^{-3}; high-temperature (dotted-dashed) component $T = 6 \times 10^7$ K, $EM = 4 \times 10^{46}$ cm^{-3}. These parameters also fit the HXRBS data at energies $E \lesssim 90$ keV. The solid line is the sum of both contributions.

fits to the HXRBS data. The high temperatures obtained from the analysis of the HXIS data before the impulsive peak have large errors, due to low count rates and the fact that the ratio between bands 5 and 6 is rather insensitive to T at these high temperatures. Still, the agreement between HXIS and HXRBS data is reasonably good.

Strikingly, we find that at $9^h18^m37^s$, that is during the hard X-ray peak, *the temperature obtained from the HXIS data decreases, while that of the HXRBS increases*. This fact reflects a change in the spectral shape from a thermal to an approximate power-law distribution, with index $\gamma = 5$ as derived from HXIS, or $\gamma = 5.4$ as obtained from the HXRBS data. Such a high value in the spectral index implies a softening in the spectrum as seen by HXIS (i.e., a temperature decrease) and a hardening at higher energies of the HXRBS data (i.e., an increase in the effective T).

Later, about one minute after the peak in the hard X-rays, both the HXIS and HXRBS data can be fitted with a high temperature component with $T = 6 \times 10^7$ K and emission measure $EM = 4 \times 10^{46}$ cm^{-3}. The actual two-temperature fit to the HXIS data within this time interval is shown in Figure 7. It should be noted, however, that a better fit to the HXRBS data could be obtained through a power-law with $\gamma = 6.5$.

A multithermal character of the flare emission is implied by the data throughout the flare, well into the decay phase. However, the existence of very hot sources is not. At 9^h21^m UT the 16 to 30 keV count rates in the coarse field of view are too low to enable us to make a statisticaly significant analysis. Still, from the more efficient HEM we infer the presence of a high temperature component with $T \approx 4 \times 10^7$ K and $EM \approx 2.5 \times 10^{47}$ cm^{-3}. At later times even this component seems to disappear, coincident with the drop in the high energy count rates of the fine field of view plots of Figure 2b. At 9^h23^m, just after the soft X-ray maximum, there is no clear evidence of the existence of a high-T component. It is most likely that discrepancies with single temperature fits are, from this time on, due to the superposition of individual loop structures at different cooling stages (see Antiochos, 1980, for a detailed analysis of flare radiative cooling and emission measure distributions).

6. Energy Dissipation and Cooling

As mentioned before, spectral fits are not very powerful in terms of discriminating between models of hard X-ray emission. What is clearly needed is a set of clear-cut predictions by theoretical models on observable quantities, so that these can be used as discriminators. Attempts along these lines have recently been made by Brown *et al.* (1980), Brown and Hayward (1981), and Emslie (1981) for comparison between the dissipative thermal model (DTM, Brown *et al.*, 1979; Smith and Lilliequist, 1979; Emslie and Brown, 1980; Smith and Auer, 1980) and the nowadays classical non-thermal (NT) thick-target model in which true acceleration takes place (Brown, 1971; Lin and Hudson, 1976; Kane *et al.*, 1980, and references therein).

We now turn to the spatial distribution of the hard X-ray emission which was qualitatively described in Section 4. We can summarize the properties of the 16 to 30 keV emission as follows:

(a) *Pre-burst phase:* It seems to originate mainly from the location of pixels 4, 5, and 9 (cf., Figure 2) with only a minor contribution from the others. This implies that most photons are produced within the small loop structure that was inferred from the overlay of HXIS and UVSP images and magnetic field data.

(b) *Hard X-ray burst:* As shown before, the emission of footpoints exceeds the loop emission by a factor ≥ 2 in the 16 to 30 keV range, and is ≈ 1 in the 11.5 to 16.0 keV interval (B4). This latter value is also a lower limit, since the contribution from the soft X-ray plasma within the loop has not been subtracted.

(c) *Post-burst phase:* The emission is concentrated in loop pixels, with very little contribution from the footpoints. The location of maximum brightness shifts from pixel 8 to 11 (i.e., westwards) as time progresses.

In phases (a) and (c) one can most likely postulate that the observed emission is thermal, with temperatures and emission measures approximately characterized by the values given in Table I. Phase (b), however, the most important for discrimination between the DTM and NT models, seems to support the latter, as shown below.

6.1. Impulsive burst

We note, first of all, that the duration of the footpoint brightenings is of the order of 20 s (FWHM), implying a continuous injection of high energy electrons into the target for a comparable length of time. In terms of the DTM, this implies a continuous regeneration of the high energy tail of electrons which escapes through the ion-acoustic turbulent fronts, or conversely, the successive creation of a large number of thermal regions, as envisioned by Brown *et al.* (1980) and Brown and Hayward (1981). In both cases the DTM encounters serious difficulties, since processes capable of regenerating the tail within a fraction of a second, and even creating it in the first place, have not been worked out in detail (see, e.g., Vlahos and Papadopoulos, 1979).

The brightness ratio between footpoint and loop structures should also, in principle, be a good discriminator. Emslie (1981) has computed the height distribution of hard X-rays in thick-target and thermal models. For acceptable DTM parameters ($n = 10^{11}$ cm^{-3}, $T_e = 22.2$ keV) and assuming that electrons with velocities $v \geq 3v_e$ can escape through the turbulent ion-acoustic fronts of the DTM (see Brown *et al.*, 1979; Smith and Lilliequist, 1979), v_e being the electron thermal velocity, he finds that at 40 keV a HXIS-like pixel observing the thermal region should be a factor between 1.5 to 2 times brighter than a footpoint pixel. At lower energies, of more relevance to HXIS, this factor increases, being > 10 at 10 keV. These expected ratios are in contradiction to the observations of the April 10 flare.

It should be mentioned that accurate model discrimination is hampered by several limitations. From the observational point of view, a more detailed knowledge of the HXIS fine field of view transmission properties is needed (cf. remarks in Section 5) to be able to obtain accurate spectral properties of localized flare regions. From the theoretical viewpoint, the energy distribution of the tail electrons as well as their low energy cutoff are uncertain. Both Maxwellian and power-law tails have been assumed (Brown *et al.*, 1980; Brown and Hayward, 1981; Emslie, 1981) and the parameter β, where $v = \beta v_e$ is

the escape velocity of electrons through the fronts, is largely unknown. All these factors render the analysis in terms of the DTM rather uncertain.

The NT model assumption does not seem to encounter any serious difficulty. It always predicts high brightness contrasts in favor of the footpoints, although the total X-ray yield as function of height is dependent on the atmospheric structure (cf., results by Emslie (1981), who used flare model atmospheres compared to those of Brown and McClymont (1975), who assumed a quiet Sun target).

Bearing in mind the uncertainties in the DTM, we can make a simplified analysis in terms of this and the NT model.

For a DTM, the ratio between thick target and thermal emission is (Emslie and Vlahos, 1980; Emslie, 1981)

$$\eta(\varepsilon) = \begin{cases} \dfrac{6.6 \times 10^{11}}{nL} \dfrac{\beta^4}{4(\delta-2)} e^{-\beta^2/2} e^{\varepsilon/kT} (kT)^2 \ln\left(\dfrac{2\beta^2 kT}{\varepsilon}\right) & \text{for} \quad \varepsilon < E_{\min}\,, \quad (1a) \\ \infty \quad \text{for} \quad \varepsilon \geq E_{\min}\,, & (1b) \end{cases}$$

where ε is the photon energy, δ is the power-law index in the particle spectrum for $v \geq \beta v_e$, which we assume $= 6$ following the HXRBS and HXIS results, $n\,(\mathrm{cm}^{-3})$, $T\,(\mathrm{K})$, and $L\,(\mathrm{km})$ are the density, electron temperature, and length of the thermal source. We assume, following Emslie (1981), $\beta = 3$, and $E_{\min} = \frac{1}{2}\beta^2 kT$ is the threshold energy of escaping electrons.

Following our results we assume $\eta\,(20\ \mathrm{keV}) = 2$ and $\eta\,(12\ \mathrm{keV}) = 1$ as lower limits. Simple calculations show that the best fit parameters are $T \approx 1.2 \times 10^8\ \mathrm{K}$ and $nL \approx 3 \times 10^{13}\ (\mathrm{cm}^{-3}\ \mathrm{km})$ with large uncertainties. We should bear in mind that these are the most favorable parameters in terms of the DTM. Still, for these values the ratio of the thermal region length to the collisional mean free path of a thermal electron, the parameter Δ of Brown *et al.* (1980), is $\Delta \approx 3 \times 10^{-3}$. For these low values of T and Δ the DTM looses its advantage in terms of efficiency compared to the NT case. Actually, considering the fact that a high energy tail has to be continuously generated, the model has no substantial difference with one which involves acceleration.

In terms of a thick-target (NT) process, the photon flux at 1 AU is given by (Hoyng *et al.*, 1976, with a minor numerical correction)

$$I_{tt}(\varepsilon) = \frac{F(\varepsilon)}{2.62 \times 10^{33} (\gamma-1)^2 B(\gamma - \frac{1}{2}, \frac{1}{2})}\ \mathrm{ph\ cm^{-2}\ s^{-1}\ keV^{-1}}\,, \quad (2)$$

where $F(\varepsilon)$ is the number of electrons with energies greater than ε that precipitate into the target, B is the beta function, and γ the photon spectral index. Both the HXIS and HXRBS observations show that $I\,(20\ \mathrm{keV}) = 20$ to $30\ \mathrm{ph\ cm^{-2}\ s^{-1}\ keV^{-1}}$ at the peak of the event. Assuming $I\,(20) = 25\ \mathrm{ph\ cm^{-2}\ s^{-1}\ keV^{-1}}$ we find that the peak value for both footpoints summed is $\approx 16.7\ \mathrm{ph\ cm^{-2}\ s^{-1}\ keV^{-1}}$ (where we have subtracted $\frac{1}{3}$ of

the emission coming from loop pixels). Replacing in (2) we find, for $\gamma = 5.5$, that

$$F(20) = 7.2 \times 10^{35}\ \mathrm{s}^{-1} \tag{3}$$

and the power in accelerated electrons is

$$P(20) = 2.8 \times 10^{28}\ \mathrm{erg\ s}^{-1}\,. \tag{4}$$

Taking a peak FWHM = 20 s we find

$$\int P(20)\,\mathrm{d}t = 5.6 \times 10^{29}\ \mathrm{erg} \tag{5}$$

as the energy deposited by the beam. This value is an upper limit, since we have taken peak values for the flux and a constant index. As we shall see below, this is only a fraction of the total flare energy.

6.2. Gradual phase

Both in the soft and harder X-rays we can define gradual phases in their light curves. In the soft X-rays this has been described as the thermal phase of the flare, in which the emission measure reaches a maximum and slowly decays together with the temperature of the emitting plasma.

The total thermal energy of the flare X-ray plasma at a given instant is

$$E_{\mathrm{th}} = \frac{3EMkT}{n}\,. \tag{6}$$

At the peak in the softer X-rays, assuming an electron density $n = 10^{11}\ \mathrm{cm}^{-3}$, which is consistent with the observed emission measure and a volume $V \approx 6 \times 10^{26}\ \mathrm{cm}^3$ ($3 \times 1 \times 1$ HXIS pixels) we obtain $E_{\mathrm{th}} \approx 2 \times 10^{30}$. This is a lower limit, since we know from BCS data that there is a large amount of material at lower temperatures than those shown in Figure 5 (Antonucci *et al.*, 1982). Including BCS estimates the energy rises to $E_{\mathrm{th}} \gtrsim 3 \times 10^{30}$ erg (note the strong dependence on the density assumed).

The radiative output of the flare is obtained from

$$E_{\mathrm{rad}} = \int \Phi(T)\, EM(t)\,\mathrm{d}t\,, \tag{7}$$

where $\Phi(T)$ is the radiative loss function (Raymond *et al.*, 1976). From the values of Figure 5 we obtained $E_{\mathrm{rad}} = 3 \times 10^{29}$ erg. The BCS results indicate $E_{\mathrm{rad}} = 2 \times 10^{30}$ erg. A comparable amount of radiative power should be provided by EUV radiation in lower temperature lines and strong visible lines, mainly Hα. Therefore the total E_{rad} should be $> 2 \times 10^{30}$ erg.

Comparing radiative and conductive cooling times, we find

$$\tau_{\mathrm{rad}} = \frac{3kT}{n\Phi(T)} = 4 \times 10^3\ \mathrm{s}\,, \tag{8}$$

$$\tau_{\text{cond}} = \frac{3nkL^2}{\varkappa} \approx \frac{3 \times 10^{-10}\, nL^2}{T^{5/2}} = 67 \text{ s}, \tag{9}$$

where we have again assumed $T = 2 \times 10^7$ K, $n = 10^{11}$ cm^{-3}, and estimated the loop length $L = 2 \times 10^9$ cm.

Even when these estimates are quite crude, it is clear that the conductive time scale is too short compared to the lifetime of the flare. If conduction was the main cooling mechanism the results would imply a continuous energy release throughout the lifetime of the flare, increasing its energy budget by about two orders of magnitude. This is very unlikely, both on theoretical grounds and from the fact that eventually the conductive flux should be radiated away by the low temperature plasma. No such evidence exists from chromospheric and transition line observations (see, e.g., Švestka, 1976; Krieger, 1979; Canfield *et al.*, 1980).

Cheng and Widing (1975) suggested that conduction might be inhibited by anomalous processes as those arising in DTM (cf. references in Section 6.1), i.e., by increased plasma turbulence due to the excitation of waves. Krieger (1979) checked this possibility for a variety of flares and found that when soft X-ray parameters were assumed the flare loops were well within the range of stability for classical processes.

The classical heat flux can be expressed as

$$Q_{\text{cl}} \approx 0.96 \frac{k^{5/2}}{\sqrt{m_e}\, e^4} \frac{T^{5/2}}{\ln \Lambda} \frac{kT}{L} \tag{10}$$

and the saturated

$$Q_{\text{sat}} \approx \frac{1}{4} nmv_e^3 \approx \frac{1}{4} \frac{(kT)^{3/2}}{\sqrt{m_e}}. \tag{11}$$

After some algebra, we obtain

$$\frac{Q_{\text{cl}}}{Q_{\text{sat}}} \approx 6.9 \times 10^4 \frac{T^2}{nL}. \tag{12}$$

Assuming again that $n = 10^{11}$ cm^{-3} and $L = 2 \times 10^9$ cm, we find that $Q_{\text{cl}}/Q_{\text{sat}} = 0.14$ so that the flare loop is within the range of classical heat conduction.

In the harder X-rays, at energies above 16 keV, we can also define a gradual phase of the flare emission. Both before and after the impulsive burst we observe a considerable number of counts in the HXIS energy bands 5 and 6 and in the HXRBS records. These photons could be produced by a thick-target process or by thermal emission from a hot plasma. Two reasons lead us to believe in the second possiblity.

First of all, a continuous thick-target process would imply a large increase in the flare energy budget, leading to the same problem as with the conductive cooling. Second, and more relevant to the observational evidences given by HXIS, we see different structural

details in the pre- and post-burst phases. The emission at these times is spatially related to loop structures, with a minimal fraction originating at the footpoints.

A thin-target type of a process can also be discarded. At high densities the relaxation times for high energy electrons are too short, and lower densities would imply a large magnetic bottle in contradiction to the discrete source appearance in the HXIS images (cf. shift in the location of brightness maxima from pixel 8 to 11). Continuous reacceleration is also unlikely, for energetic reasons and, again, localized appearance in the HXIS images.

Assuming then that real, hot, thermal sources exist within the flare loops, we can examine their properties.

We define two particular times for our analysis (see Table I):

(a) Pre-burst phase, $t-1$, with characteristic parameters $EM = 5 \times 10^{45}\ \mathrm{cm}^{-3}$ and $T = 1.2 \times 10^{8}\ \mathrm{K}$.

(b) Post-burst phase, $t-2$, with parameters $EM = 4 \times 10^{46}\ \mathrm{cm}^{-3}$ and $T = 6 \times 10^{7}\ \mathrm{K}$.

The characteristic length of these regions is unknown, but since we have seen before that neighboring loop pixels show different temporal characteristics in the high energy bands we assume $L = 6 \times 10^{8}$ cm (a HXIS pixel). We assume $n = 10^{11}\ \mathrm{cm}^{-3}$, noting that if the region was in pressure equilibrium with its surroundings the most likely value would be $n = 10^{10}\ \mathrm{cm}^{-3}$. In terms of the length L, we could either have a small hot region or a conglomerate of hot threads within the area of one pixel. Our observations do not allow us to discriminate between these two possibilities.

Radiative cooling processes are unimportant in these hot regions, since $\tau_{\mathrm{rad}} \gtrsim 10^{4}$ s.

As for conductive processes we find that:

$$t-1: \quad Q_{\mathrm{cl}}/Q_{\mathrm{sat}} \approx 16.6\,,$$

$$t-2: \quad Q_{\mathrm{cl}}/Q_{\mathrm{sat}} \approx 4.2\,.$$

Both these values represent lower limits, as can be seen from Equation (12) and the physical parameters assumed.

In the case of a saturated heat flux, the conductive times are:

$$t-1: \quad \tau_{\mathrm{cond}}\,(\mathrm{sat}) \approx 1.1\ \mathrm{s}\,,$$

$$t-2: \quad \tau_{\mathrm{cond}}\,(\mathrm{sat}) \approx 2\ \mathrm{s}\,.$$

Anomalous processes could further limit the conductive flux. These have been estimated for the DTM under the condition of $T_e/T_i \gg 1$ (see, e.g., Smith and Lilliequist (1979); when electron and ion temperatures are comparable the anomalous processes may have a different threshold).

The anomalous heat flux is given by

$$Q_{\mathrm{an}} = \tfrac{3}{2} n m_e v_e^2 v_f\,, \tag{13}$$

where v_f is the speed of the conduction front which at the limit when $T_e/T_i \to \infty$ becomes

the ion-sound speed v_s. A maximum value of τ_{cond} can then be obtained from

$$\tau_{\text{cond}}\,(\text{an}) = \frac{1}{2}\sqrt{\frac{M}{m_e}}\,\frac{L}{v_e} \tag{14}$$

which gives ≤ 3 s and ≤ 4.3 s for the two times considered.

It is thus clear that continuous energy release is needed to sustain the hot thermal regions. Their energy content can be calculated from (6) to be:

$$t-1: \quad E_{\text{th}} \geq 2.5 \times 10^{27} \text{ erg},$$

$$t-2: \quad E_{\text{th}} \geq 10^{28} \text{ erg}.$$

These values could be underestimated by about one order of magnitude, and keeping in mind that we find evidences for the existence of these regions for a period of ≈ 4 min, we find that $> 10^{30}$ erg are released throughout their lifetime.

7. Discussion

We have shown the characteristics of the 3.5 to 30.0 keV emission in a solar flare. Our results can easily be compared with those reported by Hoyng *et al.* (1981b) for a large two-ribbon event of May 21, 1980 and, in qualitative terms, are similar to several others recorded by the HXIS.

In agreement with the Hoyng *et al.* (1981b) results we find that the hard X-ray emission can be decomposed in two clearly defined components. The impulsive short-lived component showing up at high energies in the HXRBS data and footpoint structure in the HXIS images. A 'gradual' component, lasting for a period of few minutes in the April 10 flare, and longer in the May 21 two-ribbon type, which is spatially localized within loop structures embedded in the bright soft X-ray region. Prior to the impulsive burst we also see evidences for localized high energy emission within loop structures.

As in the discussion by Hoyng *et al.* (1981b), we find that a dissipative thermal model assumption for the hard X-ray burst does not give the appropriate parameters to make it an efficient alternative to the non-thermal model. Therefore, particle acceleration does seem to take place during the impulsive phase.

In the gradual phase in hard X-rays, before and after the impulsive burst, we conclude that most of the hard X-ray emission is of thermal origin. A crude analysis was made showing that the energy dissipated during the lifetime of the hot regions is of the same order of magnitude as the total flare energy release. In this respect we can compare our results with those of Antonucci *et al.* (1981). They showed that, for a period that overlaps with that in which hot regions exist, there is a continuous energy input in the soft plasma and strong evaporation, as evidenced by blue shifted components in the emission lines (see also results by Doschek *et al.*, 1979). Antonucci *et al.* find that the enthalpy and kinetic energy of the blue-shifted plasma, which is introduced into the loop structures, is of the order of 3.7×10^{30} erg, accounting for the total energy estimated at flare maximum, just after the evaporation stops. Therefore, the energy and mass input is found to be able to account for the flare parameters at maximum and decay phases if the latter

is dominated by radiative cooling. The driver of this process may be the energy dissipated from the hot regions.

The following qualitative flare picture emerges from these observations:

(a) *Pre-heating phase:* short-lived and localized, preceeding the impulsive phase. High-temperature plasmas are produced and the emission measure in the softer, low-temperature, component begins to rise.

(b) *Impulsive phase:* associated with particle acceleration and occurring only within particular magnetic structures.

(c) *Gradual phase in the hard X-rays:* continuous energy release for a period of minutes and production of high-temperature region whose cooling is dominated by saturated heat flux, possibly limited by anomalous processes. The energy is transferred to the soft plasma which evaporates from the chromosphere as long as the energy release continues.

(d) *Gradual phase in the soft X-rays:* after phase (c) when the energy release and strong evaporation ceases.

The subsequent cooling seems to be dominated by radiative processes, as discussed by Antiochos (1980).

Phases (a) and (c) are probably manifestations of the same phenomenon, over which phase (b) is superimposed. The energetic importance of phase (b) is not clear. The numbers quoted in Section 6.1 are substantially lower than the total flare energy budget but, if the lower energy cutoff of the accelerated electron population was ≈ 10 keV, the two numbers could become comparable. It is in any case evident that long-lasting energy release is needed, with characteristics that do not support a continuous thick-target model. The Hoyng *et al.* (1981b) results are more clear in this respect, since even taking a lower energy cutoff the energy budget in accelerated electrons is much less than the total flare energy release. The main difference between these two flares lies in that the large two-ribbon case of May 21 shows evidences of continuous energy release over a much longer period. This difference may be related to the fact that in such a case we see (as suggested by Hoyng *et al.*) continuous reconnection of open field lines, while in the more compact April 10 event the release is confined within discrete, closed, magnetic structures.

Several subjects remain open for further research and for confirmation of our results. Of these, the existence and origin (production) of the hot regions is crucial. It should be noted that similar results were obtained by Sylwester *et al.* (1980), in their differential emission measure analysis of a large flare observed by the INTER-COSMOS-4 satellite without spatial resolution. Continuous production of hot regions is needed, a way to investigate their production rate would be through high time resolution observations during the gradual phase (c) in the hard X-rays.

We have completely neglected in our analysis the study of the characteristics of the second, hard, burst at $9^h20^m50^s$ (Figure 4). Such a feature is fairly common in our records. Two better cases, in terms of count statistics, were obtained from flares on May 9 and November 5, 1980 and in both cases the second burst seems to be located within loop structures, as it is the case in the April 10 flare (cf. Section 4).

The spatially resolved hard X-ray records should be carefully studied in connection

with magnetic field measurements. As we have seen, only one of the apparent structures participating in the flare showed impulsive burst behavior. The characteristics of such a structure should be determined to gain insight into the conditions under which acceleration may take place.

The HXRBS records often show in phase (c) that a high energy tail appears added to the softening spectrum at lower energies (Dennis *et al.*, 1981). The April 10 flare is no exception and the excess is evidenced by the better fit of a power-law at high energies during the gradual phase, as mentioned in Section 5.2. This high energy tail may be due to second stage acceleration or to the evolution of the electron distribution in a large trap. In support to this second possibility we note that during the late decay phases of this and other events observed in the same region, the HXIS observed a high altitude soft X-ray feature extending throughout the whole active region, from the leader to trailer spots.

Acknowledgements

The development and construction of the Hard X-Ray Imaging Spectrometer was sponsored by the Netherlands Comittee for Geophysics and Space Research (GROC) of the Royal Netherlands Academy of Sciences (KNAW), and The Science Research Council of United Kingdom.

A great deal of people involved in the SMM project at Goddard Space Flight Center contributed to the results presented in this paper. Our special thanks are due to E. Antonucci from XRP, R. Shine from UVSP and D. Rust, our efficient observatory coordinator.

Peter Hoyng contributed substantially to the study and he deserves a lot of credit for the ideas presented in this paper.

We also thank M. Galama, F. Werkhoven, N. Walpole, and F. Schoo Lastra for technical assistance.

References

Acton, L. W., Culhane, J. L., Gabriel, A. H., and 21 co-authors: 1980, *Solar Phys.* **65**, 53.

Antiochos, S. K.: 1980, *Astrophys. J.* **241**, 385.

Antonucci, E., Gabriel, A. H., Acton, L. W., Culhane, J. L., Doyle, J. G., Leibacher, J. W., Machado, M. E., Orwig, L. E., and Rapley, C. G.: 1982, *Solar Phys.* **78**, 107.

Brown, J. C.: 1971: *Solar Phys.* **18**, 489.

Brown, J. C.: 1972, *Solar Phys.* **26**, 441.

Brown, J. C. and Hayward, J.: 1981, *Solar Phys.* **73**, 121.

Brown, J. C. and McClymont, A. N.: 1975, *Solar Phys.* **41**, 135.

Brown, J. C., Melrose, D. B., and Spicer, D. S.: 1979, *Astrophys. J.* **228**, 592.

Brown, J. C., Craig, I. J. D., and Karpen, J. T.: 1980, *Solar Phys.* **67**, 143.

Canfield, R. C., Cheng, C. C., Dere, K. P., Dulk, G. A., McLean, D. J., Robinson, R. D., Schmahl, E. J., and Schoolman, S. A.: 1980, *Solar Flares – A Monograph from Skylab Solar Workshop II*, Boulder, Colorado Univ. Press (Appendix A).

Cheng, C. C. and Widing, K.: 1975, *Astrophys. J.* **201**, L735.

Crannell, C. J., Frost, K. J., Mätzler, C., Ohki, K., and Saba, J. L.: 1978, *Astrophys. J.* **223**, 620.

Dennis, B. R., Frost, K. J., Kiplinger, A. L., and Orwig, L. E.: 1980, *Bull. Am. Astron. Soc.* **12**, 901.
Elcan, M. J.: 1978, *Astrophys. J.* **226**, L99.
Emslie, A. G.: 1981, *Astrophys. J.* **245**, 711.
Emslie, A. G. and Brown, J. C.: 1980, *Astrophys. J.* **237**, 1015.
Emslie, A. G. and Vlahos, L.: 1980, *Astrophys. J.* **242**, 359.
Hoyng, P., Brown, J. C., and van Beek, H. F.: 1976, *Solar Phys.* **48**, 197.
Hoyng, P., Machado, M. E., Duijveman, A. *et al.*: 1981a, *Astrophys. J. Letters* **244**, L153.
Hoyng, P., Duijveman, A., Machado, M. E. *et al.* : 1981b, *Astrophys. J. Letters* **246**, L155.
Kane, S. R., Crannell, C. J., Datlowe, D., Feldman, U., Gabriel, A., Hudson, H. S., Kundu, M. R., Mätzler, C., Neidig, D., Petrosian, V., and Sheeley, N. R., Jr.: 1980, *Solar Flares – A Monograph from Skylab Solar Workshop II*, Boulder, Colorado Univ. Press.
Krieger, A. S.: 1978, *Solar Phys.* **56**, 107.
Lin, R. P. and Hudson, H. S.: 1976, *Solar Phys.* **50**, 153.
Mewe, R. and Gronenschild, E. H. B. M.: 1981, *Astron. Astrophys. Suppl.* **45**, 11.
Moore, R., McKenzie, D. L., Švestka, Z., Widing, K. G., Antiochos, S. K., Dere, K. P., Dodson-Prince, H. W., Hiei, E., Krall, K. R., Krieger, A. S., Mason, H. E., Petrasso, R. D., Pneuman, G. W., Silk, J. K., Vorpahl, J. A., and Withoe, G. L.: 1980, *Solar Flares – A Monograph from Skylab Solar Workshop II*, Boulder, Colorado Univ. Press.
Orwig, L. E., Frost, K. J., and Dennis, B. R.: 1980, *Solar Phys.* **65**, 25.
Pallavicini, R. and Vaiana, G. S.: 1980, *Solar Phys.* **67**, 127.
Peterson, L. E. and Winkler, J. R.: 1959, *J. Geophys. Res.* **64**, 697.
Raymond, J. C., Cox, D. P., and Smith, B. W.: 1976, *Astrophys. J.* **204**, 290.
Schmahl, E. J., Solodyna, C. V., Smith, J. B., and Cheng, C. C.: 1978, *Solar Phys.* **60**, 323.
Simnett, G. M., Boelee, A., Charlton, C. P., De Jager, C., Duijveman, A., Fryer, R., Galama, M., Hoekstra, R., Hoyng, P., Imhof, L. P., Lafleur, H., Machado, M. E., Maseland, J. V. A. M., Mels, W. A., Schadee, A., Schrijver, J., Švestka, Z., Van Beek, H. F., Van Rens, P., Van der Laan, J. J. M., Van Tend, W., Werkhoven, F., Wiersma, G., Willmore, A. P., Wilson, J. W. G., and Zandee, W.: 1981, in H. S. Hudson (ed.), *Adv. Space Res.* **1**, No. 13, p. 255, Pergamon Press.
Smith, D. F. and Auer, L. H.: 1980, *Astrophys. J.* **238**, 1126.
Smith, D. F. and Lilliequist, C. G.: 1979, *Astrophys. J.* **232**, 582.
Sylwester, B., Jakimiec, J., Sywester, J., and Valnicek, B.: 1981, in H. S. Hudson (ed.), *Adv. Space Res.* **1**, No. 13, p. 239, Pergamon Press.
Švestka, Z.: 1976, *Solar Flares*, D. Reidel Publ. Co., Dordrecht, Holland.
Van Beek, H. F., Hoyng, P., Lafleur, B., and Simnett, G. M.: 1980, *Solar Phys.* **65**, 39.
Van Beek, H. F., De Jager, C., Fryer, R., Schadee, A., Švestka, Z., Boelee, A., Duijveman, A., Galama, M., Hoekstra, R., Hoyng, P., Imhof, J. P., Lafleur, H., Machado, M. E., Maseland, H. V. A. M., Mels, W. A., Schrijver, J., Simnett, G. M., Van der Laan, J. J. M., Van Rens, P., Van Tend, W., Werkhoven, F., Willmore, A. P., Wilson, J. W. G., and Zandee, W.: 1981, *Astrophys. J. Letters* **244**, L157.
Van Hoven, G., Anzer, U., Barbosa, D. D., Birn, J., Cheng, C. C., Hansen, R. T., Jackson, B. V., Martin, S. F., McIntosh, P. S., Nakagawa, Y., Priest, E. R., Reeves, E. M., Reichmann, E. J., Schmahl, E. J., Smith, J. B., Solodyna, C. V., Thomas, R. J., Uchida, Y., and Walker, A. B. C.: 1980, *Solar Flares – A Monograph from Skylab Workshop II*, Boulder, Colorado Univ. Press.
Vlahos, L. and Papadopoulos, K.: 1979, *Astrophys. J.* **233**, 717.
Webb, D. F.: 1980, in M. Dryer and E. Tandberg-Hanssen (eds.), 'Solar and Interplanetary Dynamics', *IAU Symp.* **91**, 00.
Woodgate, B. E., Tandberg-Hanssen, E. A., and 12 co-authors: 1980, *Solar Phys.* **65**, 73.